Detection of Faulty Elements From Sparse Far-Field Data in Active Phased Arrays via Machine Learning

Kannan, Aparna; Onat, Nehir Berk; Yarovoy, Marco Spirito Alexander; Aslan, Yanki

DOI
10.1109/OJAP.2025.3542185

Publication date
2025

Document Version
Final published version

Published in
IEEE Open Journal of Antennas and Propagation

Citation (APA)
Kannan, A., Onat, N. B., Yarovoy, M. S. A., & Aslan, Y. (2025). Detection of Faulty Elements From Sparse Far-Field Data in Active Phased Arrays via Machine Learning. *IEEE Open Journal of Antennas and Propagation*, *6*(6), 1685-1695. https://doi.org/10.1109/OJAP.2025.3542185

Received 17 December 2024; revised 5 February 2025; accepted 11 February 2025. Date of publication 14 February 2025;
date of current version 24 November 2025.

Digital Object Identifier 10.1109/OJAP.2025.3542185

Detection of Faulty Elements From Sparse Far-Field Data in Active Phased Arrays via Machine Learning

**APARNA KANNAN, NEHIR BERK ONAT, MARCO SPIRITO (Member, IEEE),
ALEXANDER YAROVOY (Fellow, IEEE), AND YANKI ASLAN**

Microelectronics Department, Delft University of Technology, 2628 CD Delft, The Netherlands

CORRESPONDING AUTHOR: N. B. ONAT (e-mail: n.b.onat@tudelft.nl)

ABSTRACT In this contribution, we analyze machine learning-assisted solutions to tackle real-time fault detection in large-scale active phased array antennas. The challenge of integrating the circuit component nonlinearities and mutual coupling effects in fault-finding methodologies is addressed. A novel machine learning (ML) solution based on an array theory-enhanced neural network (NN) is proposed. To address the practical constraints of large array measurements, sparse far-field (FF) measurements are considered. The method is experimentally verified by applying it to fault detection in a 64-element planar phased array prototype operating at 26 GHz with far-field measurements collected by a fixed high-speed multi-probe pattern acquisition setup, the Antenna Dome. Significant improvement in fault prediction performance over a conventional Genetic Algorithm (GA) based heuristic approach with improvements of up to 40%, 25%, and 20% in predicting 8-, 4-, and 2-element faults, respectively, is demonstrated. The robustness of the proposed performance with respect to the number of 3D spatial field sampling points is shown, offering efficient diagnostics with in-field pattern sampling compatibility and low hardware complexity.

INDEX TERMS Active antennas, fault diagnosis, machine learning, neural networks, phased arrays, sparse measurements.

I. INTRODUCTION

ACTIVE phased arrays integrate silicon-based multi-channel integrated circuits (ICs) with a large number of antenna elements to control excitation amplitudes and phases for flexible beamforming [1]. They are being widely proposed for high-frequency (millimeter-wave bands and beyond) systems in various communication and sensing applications, such as cellular base stations [2], satellite terminals [3] and automotive radars [4]. In such complex antenna systems, random failures in the electromagnetic radiators, ICs or IC channels may occur while the array is manufactured or assembled, or during in-field operation. The failures may lead to undesired changes in the radiation pattern, with significant effects on the gain, beamwidth, side lobe levels (SLLs), null positions and depths [5]. Before replacing any components or taking any action to compensate for the pattern changes [6], [7], it is crucial to identify the locations of the faulty elements. The ambition is to achieve such a diagnosis in almost real-time and both in post-manufacturing and in-field scenarios, which makes the problem challenging. Moreover, the IC nonlinearities and mutual coupling effects [8], [9] in practical arrays bring additional difficulties in modeling and solving this inverse problem.

One approach for fault detection in active antennas is to monitor the temperature across the array, where low temperatures (relative to the operating temperature) indicate failure. At the IC level, diagnosis can be done by placing temperature sensors inside each multi-channel IC [10]. This increases the cost, size and consumption of the ICs. Furthermore, this only detects the faulty mechanism when it occurs at the last (PA) stage and when the failure results in the device, not absorbing current. For element-level diagnosis, the infrared thermography technique has been proposed [11], [12], which visualizes the strength of electric fields through the temperature changes on an absorption screen in front of the array. In this method, the screen causes unwanted perturbation on the radiated electromagnetic waves, while the resolution of thermal images is too low to detect fails in high-frequency antennas with small physical inter-element spacing [13]. Built-in self test (BIST) sampling at each modulator channel helps in accurately pinpointing the failure at the expense of additional system cost and complexity [14].

Another competitive and widely studied approach is to monitor the electromagnetic fields over-the-air (OTA), either in the close proximity of the array (i.e., near-field, NF), or at farther distances (i.e., far-field, FF) [15]. In NF, a movable sampling probe is used to locate the defects [16]. Depending on the array size and sampling strategy, the data collection time for a fail scenario can reach up to several hours [17]. Alternatively, sparse source reconstruction techniques can be utilized to reduce the required number of samples [18]. However, the measurement system complexity, potential alignment and probe coupling errors, and long time of pattern data collection and processing pose challenges in array diagnosis at NF. This motivates the utilization of FF in high-frequency antenna diagnosis [19], [20] for which the OTA measurement distance is practically feasible. For complexity and cost reduction in the FF measurements, amplitude-only data collection [21] and sparse sampling [22], [23] have been proposed in the literature.

The measurement techniques are complemented by various algorithms solving an optimization problem with the goal of maximizing the failure detection success ratio [24]. The examples include deterministic techniques such as the Matrix Pencil Method [25], Convex Optimization [26] and Evolutionary Algorithms such as the Genetic Algorithm (GA) [20], [21], [24]. Among them, GA-like algorithms fit the problem well due to the binary nature of the unknowns (i.e., the on-off state of the elements). However, their convergence can be very slow, especially in the case of large search space [27].

Recently, several machine-learning (ML) solutions have been proposed for real-time antenna array diagnosis [28], [29]. Nevertheless, the algorithms have only been developed for the full-wave simulated and densely sampled FF data and only for small-sized (i.e., 3×3, 4×4) arrays. In a practical array, the active components bring additional non-linear effects in each IC channel response, thus on the radiation patterns, due to load pulling among the final PAs of each chain, manufacturing tolerances, and temperature variations [30], [31]. Such effects have never been studied in the ML-oriented fault diagnosis literature. There is also a lack of knowledge in the application of ML in large-sized (e.g., 8×8) array diagnostics. Besides, ML-based array diagnosis has never been integrated with sparse pattern sampling, which is necessary for a reasonable data collection time and compliance with in-field operation.

To summarize, the novel contributions of this manuscript are:

- A novel ML-assisted real-time fault detection technique using amplitude-only sparse FF sampled data is proposed.
- The IC nonlinearities, as well as mutual coupling effects, are taken into account for the first time in the formulation and solution of this inverse problem.
- Performance of the method is verified based on the measurement of a 64-element IC-integrated phased array prototype (at 26 GHz) from NXP Semiconductors and TNO [31], [32], [33] with the fixed multi-probe measurement system at TU Delft (the Antenna Dome) [34], [35].

The GA optimization is used for benchmarking, and the superior failure detection capability of the proposed ML methodology is shown. This paper, in Sections II and IV, reuses some content from thesis [36] with permission.

The rest of the paper is organized as follows. Section II describes the benchmarked and proposed fault-finding methodologies. Section III provides the details on the Antenna Under Test (AUT) and The Antenna Dome. Section IV presents the results with performance comparisons. Section V concludes the paper.

II. PROBLEM FORMULATION AND FAULT FINDING METHODOLOGIES

A. PROBLEM FORMULATION

The fundamental FF equation of a uniform planar array with N elements can be written as:

$$F(\theta_i, \phi_i) = \sum_{n=1}^{N} E_n(\theta_i, \phi_i) w_n e^{\mathrm{jk}(x_n \sin\theta_i \cos\phi_i + y_n \sin\theta_i \sin\phi_i)} \quad (1)$$

where the embedded element pattern of the n-th element is indicated as $E_n(\theta_i, \phi_i)$ with the corresponding i-th sampling point (θ_i, ϕ_i) for the spherical observation angles θ and ϕ. Furthermore, k is the wavenumber in free space, (x_n, y_n) denotes the position, and w_n is the complex excitation coefficient of the n-th element.

To mimic the element failures, the absolute value of the n-th element weight given in (1) is presumed to be 0 ($|w_n| = 0$) for a certain number of faults, which is assumed to be known by the measured power level on the broadside. Then the ultimate goal of this work is to correctly predict the locations (x_n, y_n) of all elements with $|w_n| = 0$. This is an inverse problem, which maps a measured pattern with faulty elements to the functioning array layout. As the non-linear IC behavior and coupling effects on the IC-antenna interfaces are inevitable in the active phased arrays, the measured data (with additional errors from the measurement setup) deviates from the theoretical model in (1). The practical measured pattern can be represented in a compact form as follows:

$$F_{\mathrm{ms}}(\theta_i, \phi_i) = F(\theta_i, \phi_i) + \xi_A(\theta_i, \phi_i) + \xi_D(\theta_i, \phi_i), \quad \text{for} i = 1, \ldots, M \quad (2)$$

where M is the total number of sampling points considered in the measurement setup, $\xi_A(\theta_i, \phi_i)$ and $\xi_D(\theta_i, \phi_i)$ denote the noise-like effects introduced by the AUT and the measurement setup, respectively. As the above-mentioned noise-like effects behave in a highly non-linear fashion, with deterministic and random components and with dependency on environmental conditions, accurate modeling of them is almost impossible. Several studies consider statistical error modeling in active phased arrays [37], [38], which will fail to represent a given AUT pattern behavior accurately. Therefore, the most viable option is to collect a large amount of pattern data by varying the fail scenarios randomly and modeling such effects by utilizing ML-based techniques.

In line with common practice, the FF pattern presented in (2) can be measured densely with a one-degree interval both in θ and ϕ. This approach would enable capturing the pattern variations very accurately in different element fault scenarios. However, there will be the need for continuous measurements with mechanical control, which is complex and time consuming in collecting the pattern data. On the other hand, the nodes in a sparse and fixed pattern sampling setup (with a relatively low value of M) for fast data collection cover a particular angular region with sparsely distributed nodes. Despite the increased resolution with the number of sampling nodes, there are practical limitations that come from the node sizes and coupling between the nodes [34], [35]. This, in turn, significantly reduces the spatial resolution of the FF pattern. To capture the pattern changes, it is then important that the nodes are well-distributed over the sidelobe region and not align with the nulls of the pattern. Regarding the node distribution, a good trade-off between complexity and capturing pattern variability over all subarrays is to use a minimal angular spacing that is larger than the approximate beamwidth of the antenna array (i.e., wavelength divided by the largest antenna dimension, in radians). Due to the randomized nature of our problem and the non-linearities, there are no fixed null positions to be considered in the pattern sampling strategy. The receiver positions can then be decided based on standard circular, triangular or hexagonal sampling techniques, and the effect of the total number of receivers can be studied.

In this work, the goal is to minimize the error between the ground truth pattern, $F_{\text{ms}}(\theta_i, \phi_i)$, and the predicted pattern, $\overline{F}_{\text{ms}}(\theta_i, \phi_i)$ under the test scenarios with randomly failed elements. A heuristic approach as a benchmark method and a novel ML approach is proposed to achieve this aim. A geodesic dome with receivers located on hexagonal sampling points is utilized for pattern data collection.

B. HEURISTIC APPROACH FOR BENCHMARKING: A GLOBAL OPTIMIZER (GO)

Global optimizers (GOs) are algorithms designed to find the best possible solution (global optimum) to a problem across the entire search space rather than getting trapped in local optima. GOs, such as genetic algorithm (GA) [24], simulated annealing (SA) [39], and particle swarm optimization (PSO) [40], explore the search space more broadly, balancing exploration and exploitation to ensure a comprehensive search for the optimal solution. Therefore, they have been widely exploited in array synthesis and design problems [41], [42], where real-time implementation is generally not considered crucial.

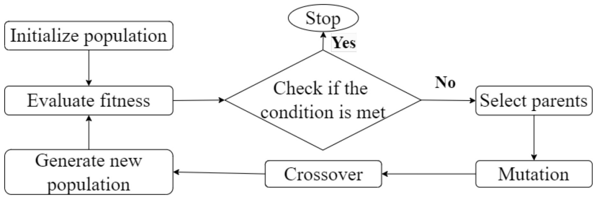

FIGURE 1. Flowchart of the Genetic Algorithm (GA).

The Genetic Algorithm (GA) is an evolutionary algorithm inspired by the principles of natural selection, iteratively evolving candidate solutions to achieve an optimal result for the given problem [43]. With its many examples in the fault finding literature (e.g., [20], [21], [24], [27]) due to its effectiveness with complex objective functions and the binary nature of the considered problem, the GA algorithm is chosen as the benchmarked heuristic approach in this paper.

As Fig. 1 illustrates, the algorithm begins by generating a population (consisting of 0s and 1s, representing the faulty and working elements, respectively), and selecting the fittest individuals from the initial population based on the defined fitness function. These selected individuals undergo crossover, where their genetic information is combined, and mutation, where random changes are introduced to create new offspring. This new generation replaces the old population, and the process repeats. Over successive generations, these update rules drive the population toward increasingly optimal solutions.

C. PROPOSED APPROACH: NEURAL NETWORKS (NNS)

ML employs data-driven methods to make predictions or decisions, and it is widely applied in various fields. ML techniques are also used in global optimization tasks such as array diagnosis, pattern recovery, and parameter estimation. The formulation of the problem, organization of data, application of algorithms, and validation of results are crucial steps in this process. Depending on the problem type, various ML methods can be utilized, including neural networks (NNs) [29], support vector machines (SVMs) [44], and others. In electromagnetics (EM) applications, machine learning is particularly effective for capturing and modeling complex, non-linear input-output relationships, which are common in EM field interactions and system behavior with IC-antenna integration. Particularly, NNs, when designed with an appropriate architecture, trained with sufficient data, and optimized using reliable techniques, can effectively approximate these relationships, enabling accurate modeling and fast prediction in complex EM scenarios.

In this work, the approach begins by incorporating the array factor equation into the loss function, ensuring that the model aligns with the basic EM principles. Since the collected measurements cannot be mathematically defined in a closed-form equation as they include multiple non-linear

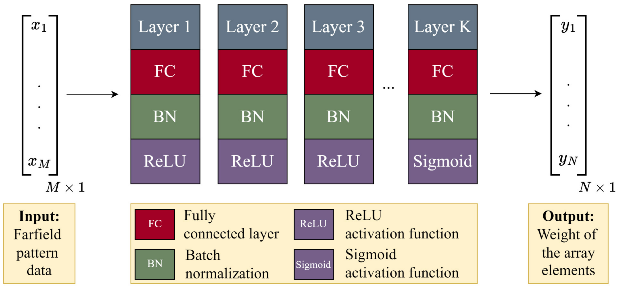

FIGURE 2. Proposed fully-connected NN architecture for detection of the faulty elements. The maximum number of layers, *K*, is initially defined as 10 for the 8-element failure case. Note that this number depends on the number of active sensor nodes, *M*.

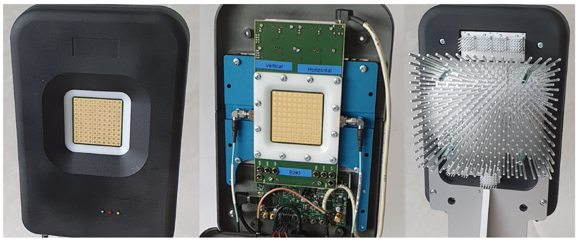

FIGURE 3. The active mm-wave (26 GHz) dual-linear polarized phased array prototyped by NXP and TNO [32], [33].

effects and setup errors, a purely data-driven model is eventually employed. Such a model is particularly well-suited for capturing the complexity of the highly intricate measurement data, which cannot be modeled by traditional EM-based methods. A fully connected NN is especially well-suited for problems where every input feature may influence every output, making it a strong choice for capturing complex, global patterns in the measured pattern data.

The proposed NN architecture consists of 10 layers, with increasing density tailored to output requirements. A probability threshold is set for class assignment in binary problems, where higher thresholds reduce false positives, and lower thresholds increase false detections. Batch normalization is applied for training stability, and dropout layers prevent overfitting. The network size is kept small to achieve the desired performance. A flowchart of the proposed architecture is illustrated in Fig. 2. The fully connected network provides the weights of the array elements $[y_1, \ldots, y_N]$ in binary form, where 0s represent faulty elements and 1s represent working elements. The initial layers have ReLU activation and the final layer uses Sigmoid activation as the desired output is binary. In this work, the TensorFlow framework is utilized.

III. ANTENNA UNDER TEST (AUT) AND PATTERN MEASUREMENT SETUP

A. THE ACTIVE MM-WAVE PHASED ARRAY UNDER TEST

The AUT is an 8×8 active phased array prototyped by NXP and TNO [32], [33]. The elements are cavity-backed patches operating at 26 GHz center frequency. The inter-element spacing is equal to half-wavelength at the center frequency. A ring of dummy elements is used at the edges for better pattern uniformity. The array is built on a 12-layer printed circuit board (PCB) and can provide dual linear polarization. Fig. 3 shows the assembled prototype with the plastic cover and heatsink at the back attached to the ICs for active cooling with a fan. The ICs are 4-channel dual-polarized analog beamforming ICs of NXP (labeled MMW9014K) operating between 24.25-27.5 GHz with 8-bit phase and gain resolution. Fig. 4 provides the schematic of the ICs, which are controlled by a Field-Programmable Gate Array (FPGA). For one polarization state, each IC channel can be independently switched on and off, or controlled with a selected gain-phase setting. The array is used with a heuristic post-manufacturing near-field calibration technique that aims

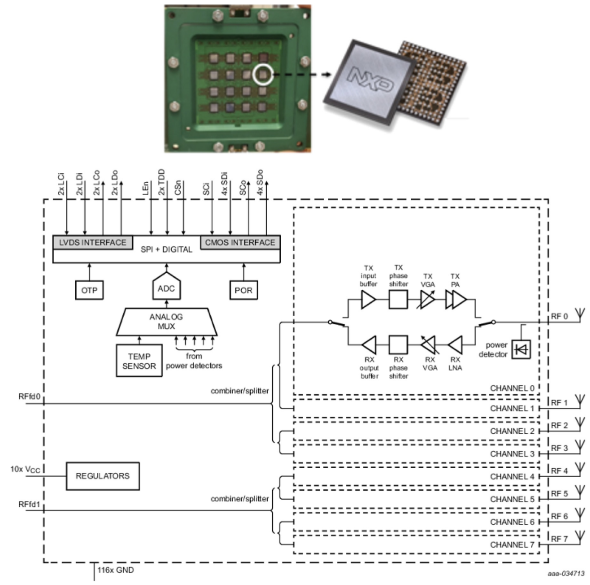

FIGURE 4. The schematic of the NXP's mm-wave beamforming IC [32].

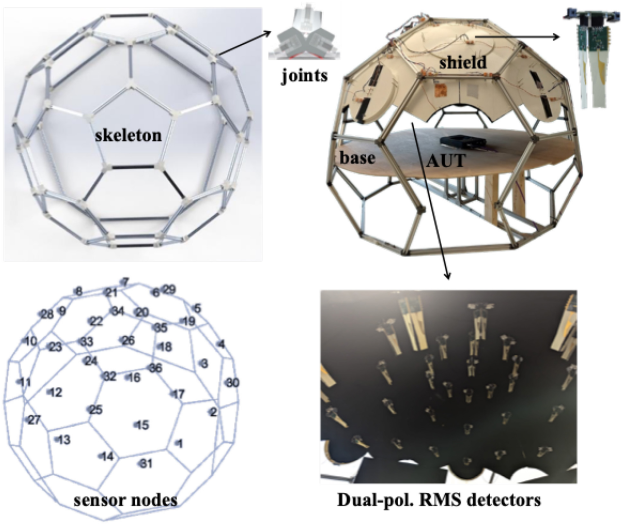

FIGURE 5. The Antenna Dome setup [34], [35], [45]: (top left) geodesic skeleton with aluminum profiles, (top right) shielded skeleton including RMS detectors and AUT; (bottom left) sensing node configuration and numbering; (bottom right) RMS detectors inside the dome.

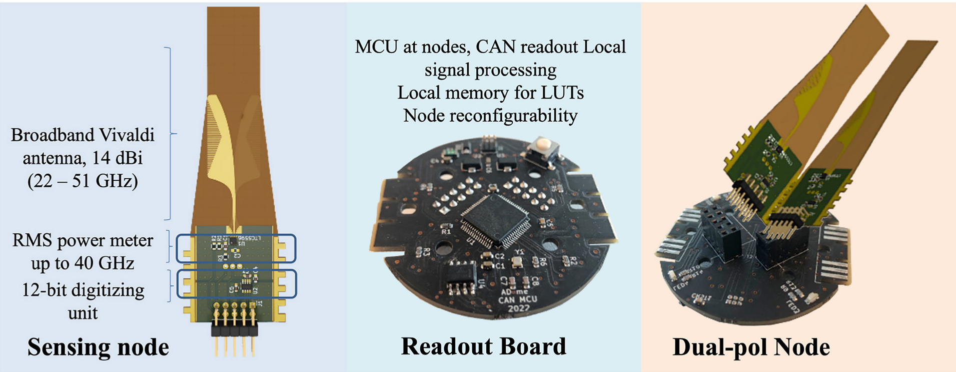

FIGURE 6. RMS detectors in the antenna board [34], [35], [45]: (left) Broadband Vivaldi antenna, 14 dBi (22 – 51 GHz), RMS power meter operating up to 40 GHz, 12-bit digitizing unit; (middle) distributed MCU, i.e., at every sensing node, providing local signal processing and memory for LUTs, CAN transceiver embedded on board; (right) illustration of the interface via DIL connectors of the orthogonally assembled sensing nodes with the readout board.

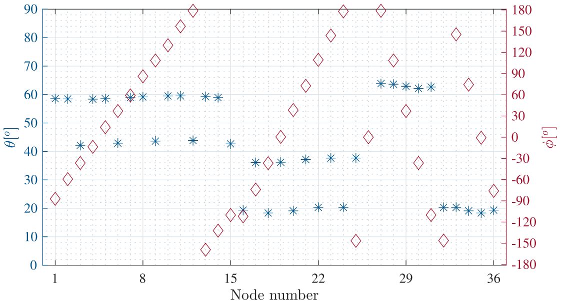

FIGURE 7. Spherical observation angle mapping of sparsely distributed 36 nodes in the Antenna Dome.

to equalize the amplitude-phase response of each element for channel imbalances [31].

In this work, a single (horizontal) polarization of the array is activated. A certain (pre-determined) number of randomly chosen IC channels are switched off to mimic the randomized element failures. This procedure is repeated while collecting a large number of pattern data associated with different topologies of the array with faults.

B. THE ANTENNA DOME

The Antenna Dome, shown in Fig. 5, is a three-dimensional (3D) array pattern acquisition setup developed at TU Delft [34], [35], [45] which removes the need for scanning equipment and greatly reduces the characterization time, at the expense of decreased pattern resolution. It has a geodesic skeleton that can be scaled using different profiles, enclosed in absorbing mounted panels to mimic an anechoic environment. In its current implementation [45], it is configured using 36 fixed dual-polarized sensing nodes. The distance between the AUT and the sensing nodes is $r = 75$ cm. The nodes cover an angular region from $\theta = 0^{\mathrm{o}}$ (broadside) to $\theta = 64^{\mathrm{o}}$ in the spherical coordinate system with a sparse distribution.

As illustrated in Fig. 6, the sensing node is a broadband Vivaldi antenna operating at 22-51 GHz, and an RMS power meter is directly integrated with the antenna with a 12-bit digitizing unit. This node is then connected to a readout board, which can locally process the received power and then send it to a computer. Each sensing node (RMS detector) provides about 40 dB dynamic range using a CAN bus architecture. The dynamic range is obtained on the detector board and is independent of the number of nodes.

The Antenna Dome initially goes through multiple calibration steps to correct for issues related to detector inter-coupling, positioning, responsivity, and polarization errors [35]. In addition, air procedures are used to address the power conversion asymmetry in dual-polarized nodes and to ensure a consistent linear response among them [35]. While the interaction between the AUT and the nodes may be inevitable, the fact that data is gathered using the same testbench setup (with identical detectors in fixed positions) means this interaction will be present in every measurement, resulting in a consistent offset across all readings. This offset can be removed through preliminary tests of the AUT performed in an anechoic chamber prior to its operation, but this topic is beyond the scope of this paper.

In this work, we utilize the Antenna Dome to collect the sparse power pattern (for a pencil beam on the broadside) of our calibrated AUT described in Section III-A while randomly turning off a pre-determined number of IC channels. The mentioned sparse power pattern is measured with the sparsely distributed receiver nodes in the Antenna Dome, where the spherical observation angle mapping of these 36 nodes is illustrated in Fig. 7. The fast-measured data is then used for testing the performance of the benchmarked GA algorithm and for training and validating the proposed ML algorithm in fault diagnosis.

IV. RESULTS

A. ARRAY THEORY-BASED TRAINING AND PREDICTION

To utilize the physics behind the problem, to observe the mutual coupling effects to some extent, and to make a transition to the data-driven models, this section considers the full-wave simulated antenna pattern data in the 64-element array, yet without integration of the ICs. The simulated embedded element pattern (EEP) of each element is included in the pattern formulation in (1), which leads to the array

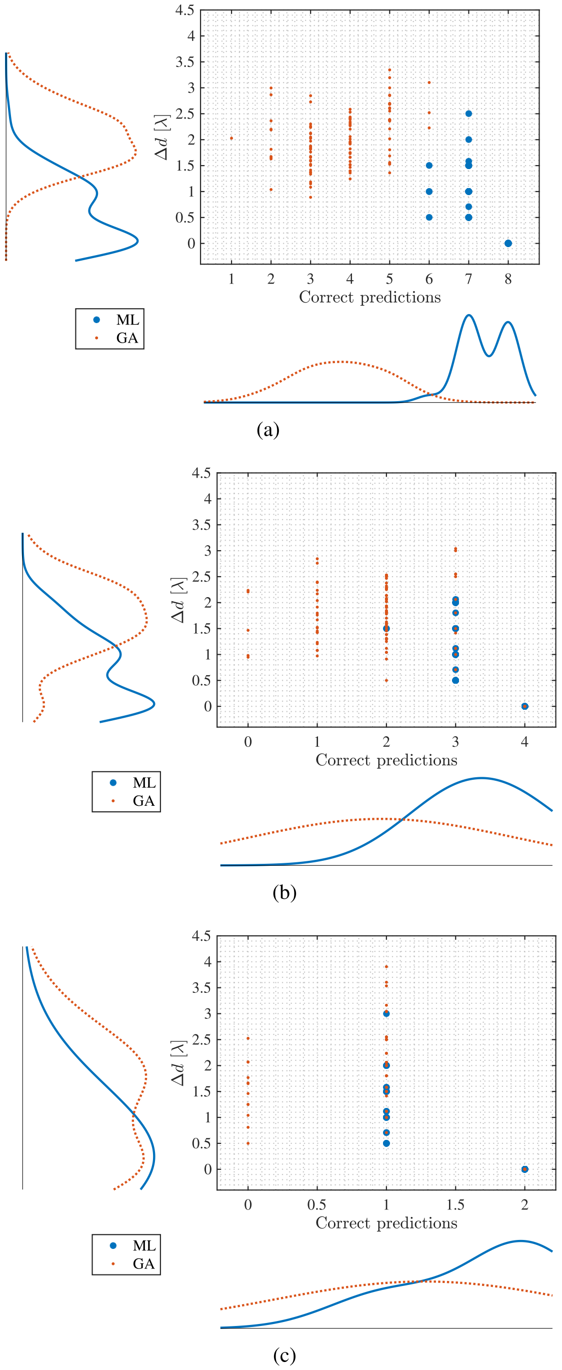

FIGURE 8. **Scatter plots with the corresponding marginal kernel densities comparing the array theory-based predictions and the GA benchmark methodology over the test set of 100 data points (based on 36 sampling points of FF simulation data). The central scatter plot illustrates the distribution of correct predictions as a function of the corresponding Δd. The smooth curves along the bottom and left margins represent the kernel density plots for the predictions of the ML model and the GA, with respect to the correct predictions and Δd, respectively. (a) 8-element failure case; (b) 4-element failure case; (c) 2-element failure case.**

theory-based training and prediction. While the NN model incorporates the FF equation, given in (1), into its loss function to enhance accuracy and generalization, having an array theory-based step also provides a fair comparison with the GA, as it requires calculating the cost function for all candidate solutions during each iteration.

TABLE 1. **GA parameter settings for the element failure prediction.**

Parameter	Value	Parameter	Value
Population size	50	Crossover probability	0.4
Number of iteration	1000	Crossover type	single-point
Number of realization	50	Mutation probability	0.1

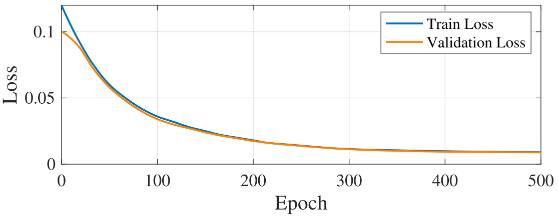

FIGURE 9. **Loss convergence plot of the proposed model for an 8-element failure sample.**

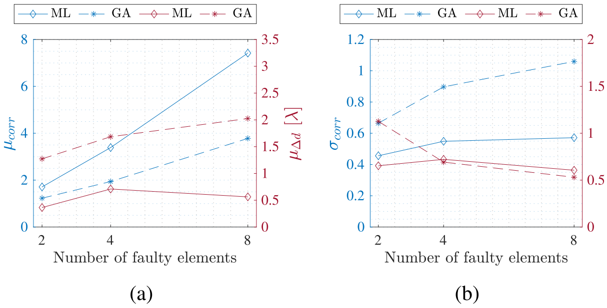

FIGURE 10. **Analyses of the average correct prediction versus the average distance between the false prediction and its ground truth with corresponding standard deviations, Δd for array theory-based prediction. (a) Average correct prediction versus average Δd over the number of faulty elements; (b) Standard deviation of the correct predictions versus standard deviation of Δd over the number of faulty elements.**

In the GA, the mean squared error (MSE) is used as a cost function to quantify the error and is employed as a fitness function:

$$\rho = \frac{1}{M}\sum_{i=1}^{M}\left(|F(\theta_i, \phi_i)| - \left|\overline{F}(\theta_i, \phi_i)\right|\right)^2 \qquad (3)$$

where M is the total number of samples, which is 36 in this case, $F(\theta_i, \phi_i)$ is the simulated ground truth pattern and $\overline{F}(\theta_i, \phi_i)$ is the predicted pattern. Tuning of the GA parameters is carried out to achieve the optimum solution to the problem. The optimized parameters are shown in Table 1.

As for the proposed NN, the FCNN architecture in Fig. 2 has layer sizes of 36 (for 36 data points), 64, and 128 at the third layer, then it reduces to 64 before thresholding at layer 10, resembling the 64x1 element weights of the AUT. The ADAM (adaptive moment estimation) is utilized as an optimizer and binary cross entropy (BCE) loss is chosen as a loss function where the model itself encourages higher probabilities for working and lower for faulty elements. Furthermore, a custom penalty function is created to penalize the network when it mispredicts the number of faulty elements.

This study analyzes three distinct failure scenarios to validate the proposed methodology. Following the standard

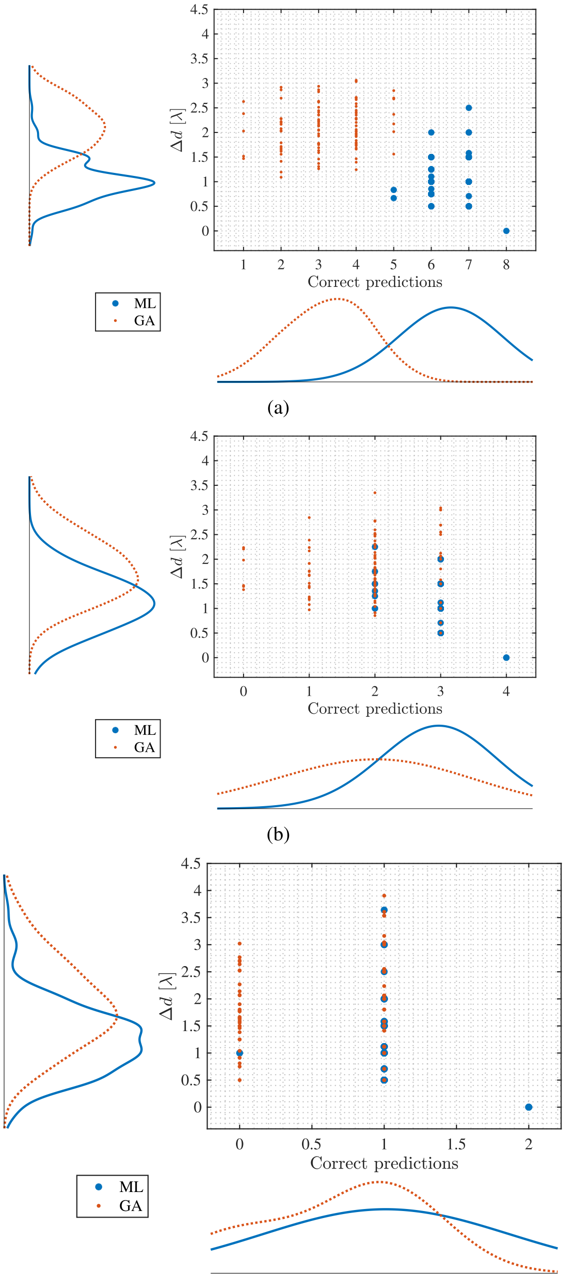

(a)

(b)

(c)

FIGURE 11. Scatter plots with the corresponding marginal kernel densities comparing the array theory-enhanced prediction and the GA benchmark methodology over the test set of 100 data points (based on 36 sampling points of FF simulation data). The central scatter plot illustrates the distribution of correct predictions as a function of the corresponding Δd. The smooth curves along the bottom and left margins represent the kernel density plots for the predictions of the ML model and the GA, with respect to the correct predictions and Δd, respectively. (a) 8-element failure case; (b) 4-element failure case; (c) 2-element failure case.

fail ratios from the literature [21], [24], an 8-element failure is initially considered, as it is expected to produce a more significant disturbance in the pattern. Subsequently, 4- and 2-element failures are investigated, where the resulting disturbances are anticipated to have a reduced impact on the pattern. It is worth noting that the number of faulty elements is assumed to be known by the measured power level. The methodologies are tested with 100 different fail scenarios randomly chosen in each case.

TABLE 2. Simulation results for array theory-based training and prediction.

nFail	Method	μ_{corr}	σ_{corr}	n_{corr}^{max}	n_{corr}^{min}	$\mu_{\Delta d}$	$\sigma_{\Delta d}$
8 El.	GA	3.78	1.06	6	1	2.03	0.53
	ML	7.42	0.57	8	6	0.56	0.60
4 El.	GA	1.94	0.90	4	0	1.69	0.69
	ML	3.39	0.55	4	3	0.71	0.72
2 El.	GA	1.23	0.66	2	0	1.27	1.13
	ML	1.71	0.46	2	1	0.36	0.65

The scatter plot in Fig. 8(a) illustrates the results for 8-element failure over the test set. The blue and red markers represent the number of correctly predicted faulty elements by ML and GA, respectively, as a function of the corresponding Δd, which denotes the distance between the false prediction and the ground truth of the mispredicted element. Furthermore, the smooth curves along the bottom and left margins represent the data densities for the predictions given in the corresponding scatter plot.

As Table 2 shows, the proposed NN methodology achieves an average of 7.42 correct predictions (μ_{corr}). Additionally, it successfully identifies the location of at least 7 out of 8 elements with 96% accuracy on the test set. On the other hand, the mean number of correct predictions (μ_{corr}) for the GA remains below 4, with a maximum correct prediction (n_{corr}^{max}) of 6 and a minimum correct prediction (n_{corr}^{min}) of 1 for the same case study due to the low number of sampling points and stochastic search nature of the GA. This significant variation in prediction accuracy is further reflected in the high standard deviation of correct predictions (σ_{corr}) across the test set.

As the number of faulty elements decreases, the disturbances in the FF pattern become less noticeable, particularly with the 36 data points, leading to a slight reduction in prediction accuracy, as shown in Figures 8(b) and 8(c). Despite this, the NN maintains a high average correct prediction rate of 3.39 out of 4, with a low standard deviation, σ_{corr}. In contrast, the GA significantly exhibits a lower μ_{corr} and a higher σ_{corr} due to the stochastic nature of the search algorithm. This trend persists in the 2-element failure case. Although prediction accuracy may decrease with fewer faulty elements, the proposed NN method can still predict the location of the misidentified faulty element within an average of a single wavelength (λ) region, as indicated by $\mu_{\Delta d}$ in Table 2, with minimal deviation of $\sigma_{\Delta d}$.

Figure 10 illustrates the behavior of the average μ_{corr} versus average Δd, along with their respective standard deviations, as a function of the number of faulty elements. While the ML demonstrates consistent performance across all numbers of faulty elements, the GA exhibits significant fluctuations with varying numbers of faulty elements, leading to reduced reliability.

B. ARRAY THEORY-ENHANCED LEARNING AND PREDICTION

The measurements collected cannot be expressed mathematically in a closed-form equation due to the presence of multiple non-linear effects brought by the ICs, IC-antenna

TABLE 3. Results for array theory-enhanced learning and prediction for measurement data.

nFail	Method	μ_{corr}	σ_{corr}	n_{corr}^{max}	n_{corr}^{min}	$\mu_{\Delta d}$	$\sigma_{\Delta d}$
8 El.	GA	3.21	1.02	5	1	2.105	0.47
	ML	6.51	0.55	8	5	1.05	0.39
4 El.	GA	1.92	0.84	3	0	1.81	0.59
	ML	2.95	0.32	4	2	1.19	0.60
2 El.	GA	0.67	0.48	1	0	1,92	0.78
	ML	1.02	0.20	2	0	1.25	0.66

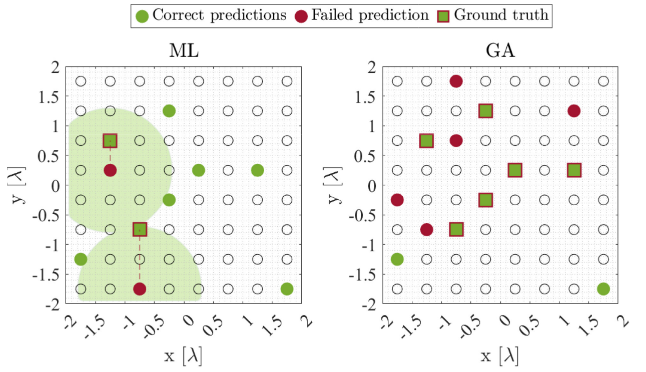

FIGURE 12. An example topology (data 70) for an 8-element failure case predicted by the proposed ML technique (left) and the heuristic approach GA (right). Black circles illustrate the antenna elements, green-filled circles indicate the correct predictions, red-filled circles indicate the failed predictions and the ground truth of the failed predictions are shown as red-framed green squares. The light green circle regions in the ML plot highlight the possible positions for the ground truth of the corresponding failed prediction.

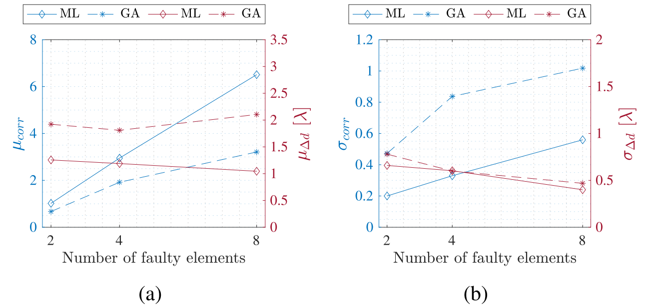

(a) (b)

FIGURE 13. Analyses of the average correct prediction versus the average distance between the false prediction and its ground truth with corresponding standard deviations, Δd for array theory-enhanced learning and prediction. (a) Average correct prediction versus average Δd over the number of faulty elements; (b) Standard deviation of the correct predictions versus standard deviation of Δd over the number of faulty elements.

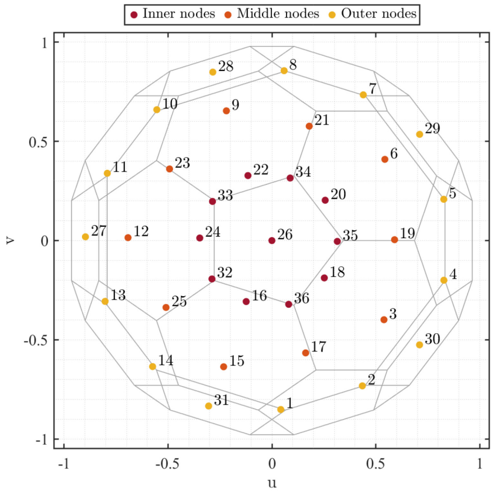

FIGURE 14. Detailed distribution of the nodes (RMS detectors) on the Antenna Dome structure. The nodes can be distributed into three different regions: inner nodes (16, 18, 20, 22, 24, 26, 32, 33, 34, 35, and 36), middle-ring nodes (3, 6, 9, 12, 15, 17, 19, 21, 23 and 25), and outer-ring nodes (1, 2, 4, 5, 7, 8, 10, 11, 13, 14, 27, 28, 29, 30, 31) which are indicated with red, orange, and yellow, respectively.

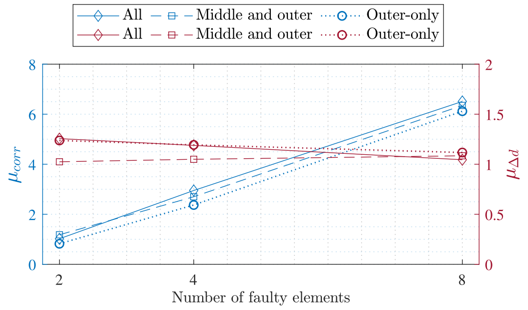

FIGURE 15. Analysis of the average correct prediction versus the average distance between the false prediction and its ground truth of the array theory-enhanced prediction for the node rings.

integration, and the measurement setup, as described in (2). To ensure that the proposed model adheres to the underlying physics of the problem, the previously presented array theory-based model is further trained with the measured data. By blending data-driven learning with the FF equation, the array theory-enhanced trained model offers a powerful approach for modeling the system where the data alone may not provide a complete understanding. In the literature, this methodology is also referred to as physics-informed neural network (PINN) [46].

The NN architecture shown in Fig. 2, is slightly modified by changing the activation function ReLU to the GeLU (Gaussian Error Linear Units), providing a smoother convergence. Furthermore, a total of 5000 measurement data is collected in approximately 30 minutes for the training and testing of the model. Among these data, 80% is used for the training, and the rest is used for validation and testing.

Since global optimizers require evaluating the cost for multiple candidate solutions across numerous generations to converge to an optimal result, the cost function must be adapted. Accordingly, the first term of the cost function in (3) now represents the measurement data corresponding to the specific failure case.

Figure 11(a), 11(b) and 11(c) illustrate the prediction results for the 8-, 4- and 2-element cases, respectively. As the measurement data introduces several nonlinearities, the number of correct predictions is slightly lower than the simulated data for the proposed methodology. While the prediction performance of the GA suffers critically, the proposed array theory-enhanced NN model obtains robust performance by achieving an average number of correct predictions of 6.51, 2.95 and 1.02 for 8-, 4- and 2-element cases, respectively.

Although the prediction accuracy appears lower in cases with fewer faulty elements, the model is still able to identify the true location of the mispredicted elements within a region of 1.5λ radius, on average with 95% accuracy. In an example case from the test data involving an 8-element failure, the proposed method successfully predicts 6 faulty elements while the GA identifies only 2 out of the 8 faulty elements (Fig. 12). Despite the model's failure to predict 2 faulty elements, these elements are located within the λ region, as highlighted in light green in Figure 12. Such errors bring minor changes in the pattern and are therefore harder to detect, yet it is possible to make a quick regional search to correct the few wrong predictions in the next iteration.

The consistency of the model over the different number of faulty elements is illustrated in Fig. 13 where the GA shows a similar behavior with the array theory-based prediction. Notably, as the number of faulty elements decreases, both the average Δd and its standard deviation decrease correspondingly.

Lastly, two more models are trained to predict the faulty elements with a low number of pattern measurement nodes. The aim of this study is to reduce the measurement setup profile towards real-time in-field data collection without blockage from absorbing panels in the field of view (FoV). To realize this, some of the RMS detectors of the Antenna Dome are disabled, and the measured data is fed into the model. Figure 14 illustrates the sampling rings corresponding to the nodes' angular positions. For this purpose, the NN architecture is adapted for different numbers of input by resizing the input and adding additional layers as described in Section II-C.

Initially, the middle and outer rings (comprising 25 nodes) are activated, followed by the activation of only the outer ring (comprising 15 nodes). Figure 15 presents the results of the proposed method for varying numbers of active nodes compared to the fully operational configuration. As the number of active nodes decreases significantly, the amount of information available for the NN to learn from also diminishes. Despite this reduction, the NN continues to perform similarly to the fully populated measurement setup.

V. CONCLUSION

This study presents a novel ML-assisted approach for real-time fault detection in large-scale antenna arrays, addressing key performance limitations in the existing methodologies against real-world complexities such as IC nonlinearities and mutual coupling effects. The architecture of the proposed NN (shown in Fig. 2) consists of K layers, where the number K depends on the size of the array and the number of probes. The new method is successfully applied to a practical 64-element phased array operating at 26 GHz, using measurement data from a multi-probe system, the Antenna Dome.

The proposed array theory-enhanced NN is capable of generating real-time predictions within seconds for the array under test, achieving better success rates of up to 40%, 25% and 20% as compared to the benchmarked heuristic (GA-based) prediction approach for 8-, 4-, and 2-element failures, respectively. The FCNN requires approximately 4 hours for training on a CPU, achieving millisecond-level prediction times, whereas the GA demands 16 hours for a single prediction on the same platform, making it significantly less efficient for real-time applications. Furthermore, while the prediction accuracy may be lower in scenarios involving fewer faulty elements, the proposed NN model remains capable of accurately identifying the possible correct locations of the mispredicted elements within an average range of one and a half wavelengths with 95% accuracy.

The study on the impact of the number of probes for pattern sampling shows minimal performance deviations when the probes near the main beam region are removed for reduced hardware and processing complexity. These advancements mark significant progress towards efficient, real-time antenna array diagnostics in practical settings, laying the groundwork for more reliable and scalable ML-assisted solutions.

In future work, using the existing setup, data collection under beam scanning and mechanical movement will be considered, and the proposed NN technique will be enhanced with real-time pattern compensation features. Moreover, the implementation of the NN-based array diagnostics framework on larger antenna sizes with potential complexity and over-fitting issues, and its application to practical near-field sparse sampling methodologies [47], [48] will be studied.

ACKNOWLEDGMENT

The authors would like to thank M. Geurts and J. Janssen from NXP Semiconductors for providing the array prototype, F. A. Musters and R. A. Coesoij from TU Delft for their previous efforts in the development of the Antenna Dome, M. Ivanyi from TU Delft for his help during the measurements, and F. Fioranelli for his assistance in improving the English grammar and readability of this paper.

REFERENCES

[1] X. Gu, D. Liu, and B. Sadhu, "Packaging and antenna integration for silicon-based millimeter-wave phased arrays: 5G and beyond," *IEEE J. Microw.*, vol. 1, no. 1, pp. 123–134, Jan. 2021.

[2] B. Sadhu et al., "7.2 A 28GHz 32-element phased-array transceiver IC with concurrent dual polarized beams and 1.4 degree beam-steering resolution for 5G communication," in *Proc. IEEE Int. Solid-State Circuits Conf. (ISSCC)*, 2017, pp. 128–129.

[3] X. Luo et al., "A scalable Ka-band 1024-element transmit dual-circularly-polarized planar phased array for SATCOM application," *IEEE Access*, vol. 8, pp. 156084–156095, 2020.

[4] C. Waldschmidt, J. Hasch, and W. Menzel, "Automotive radar—From first efforts to future systems," *IEEE J. Microw.*, vol. 1, no. 1, pp. 135–148, Jan. 2021.

[5] M. Levitas, D. A. Horton, and T. C. Cheston, "Practical failure compensation in active phased arrays," *IEEE Trans. Antennas Propag.*, vol. 47, no. 3, pp. 524–535, Mar. 1999.

[6] T. J. Peters, "A conjugate gradient-based algorithm to minimize the sidelobe level of planar arrays with element failures," *IEEE Trans. Antennas Propag.*, vol. 39, no. 10, pp. 1497–1504, Oct. 1991.

[7] F. Zaman, H. u. Hassan, S. U. Khan, A. U. Rehman, M. A. Z. Raja, and S. A. Niazi, "Backtracking search optimization paradigm for pattern correction of faulty antenna array in wireless mobile communications," *Wireless Commun. Mobile Comput.*, vol. 2019, no. 1, 2019, Art. no. 9046409.

[8] S. J. Spiegel, "Analysis of impairments, error correction and evaluation of adaptive antenna arrays based on vector modulators beamforming ICs," in *Proc. IEEE Microw., Antennas, Propag. Conf. (MAPCON)*, 2022, pp. 1255–1260.

[9] A. J. Van Den Biggelaar, C. J. C. Vertegaal, U. Johannsen, A. B. Smolders, and M. Geurts, "On the design and calibration of a 5G millimeter-wave dual-polarized active phased array," in *Proc. IEEE-APS Top. Conf. Antennas Propag. Wireless Commun. (APWC)*, 2021, pp. 55–60.

[10] Y. Aslan, C. E. Kiper, A. J. van den Biggelaar, U. Johannsen, and A. Yarovoy, "Passive cooling of mm-wave active integrated 5G base station antennas using CPU heatsinks," in *Proc. 16th Eur. Radar Conf. (EuRAD)*, 2019, pp. 121–124.

[11] D. L. Balageas, P. Levesque, and A. A. Deom, "Characterization of electromagnetic fields using a lock-in infrared thermographic system," in *Proc. 15th Thermosense Int. Conf. Therm. Sens. Imag. Diagn. Appl.*, 1993, pp. 274–285.

[12] D. Prost, F. Issac, and P. Reulet, "Large scale measurement of microwave electric field using infrared thermography and electromagnetic simulation," in *Proc. Prog. Electromagn. Res. Symp.*, 2011, pp. 1021–1024.

[13] J. Norgard and R. Musselman, "Direct diagnostic testing of phased array antennas using infrared imaging techniques," in *Proc. 17th Int. Zurich Symp. Electromagn. Compat.*, 2006, pp. 292–295.

[14] K. Muzaffar, L. I. Giri, K. Chatterjee, S. Tuli, and S. Koul, "Fault detection of antenna arrays using infrared thermography," *Infrared Phys. Technol.*, vol. 71, pp. 464–468, Jul. 2015.

[15] A. Hubrechsen and T. Van den Biggelaar, "Over-the-air techniques for measuring integrated RF electronics and antennas," *Microw. J.*, vol. 67, no. 1, p. 94, 2024.

[16] J. J. Lee, E. M. Ferren, D. P. Woollen, and K. M. Lee, "Near-field probe used as a diagnostic tool to locate defective elements in an array antenna," *IEEE Trans. Antennas Propag.*, vol. 36, no. 6, pp. 884–889, Jun. 1988.

[17] O. M. Bucci, M. D. Migliore, G. Panariello, and P. Sgambato, "Accurate diagnosis of conformal arrays from near-field data using the matrix method," *IEEE Trans. Antennas Propag.*, vol. 53, no. 3, pp. 1114–1120, Mar. 2005.

[18] H. Zhao, Y. Zhang, Q. Wan, J. Hu, and Z. Chen, "Near-field-based array failure diagnosis using sparse source reconstruction," in *Proc. Asia-Pac. Int. Symp. Electromagn. Compat. (APEMC)*, 2017, pp. 309–311.

[19] O. J. Famoriji, Z. Zhang, A. Fadamiro, Z. Khan, and F. Lin, "Active antenna array diagnosis from far-field measurements," in *Proc. IEEE Int. Conf. Integr. Circuits, Technol. Appl. (ICTA)*, 2018, pp. 38–39.

[20] J. Miao, B. Chen, X. Zhang, and Y. Chen, "An improved method of diagnosis of failed elements in arrays based on far-field radiation pattern," in *Proc. Prog. Electromagn. Res. Symp. (PIERS)*, 2016, pp. 467–471.

[21] O. M. Bucci, A. Capozzoli, and G. D'Elia, "Diagnosis of array faults from far-field amplitude-only data," *IEEE Trans. Antennas Propag.*, vol. 48, no. 5, pp. 647–652, May 2000.

[22] B. Fuchs, L. L. Coq, and M. D. Migliore, "Fast antenna array diagnosis from a small number of far-field measurements," *IEEE Trans. Antennas Propag.*, vol. 64, no. 6, pp. 2227–2235, Jun. 2016.

[23] Z. Li, P. Huo, and J. Wu, "Fast antenna array diagnosis based on shifted base mode character from sparse measurements," *IEEE Trans. Antennas Propag.*, vol. 70, no. 12, pp. 12163–12176, Dec. 2022.

[24] N. Boopalan, A. K. Ramasamy, and F. Nagi, "A comparison of faulty antenna detection methodologies in planar array," *Appl. Sci.*, vol. 13, no. 6, p. 3695, 2023.

[25] G. Bai, C. Liao, Y. Liu, and Y.-F. Cheng, "Rapid failure diagnosis of impaired linear antenna arrays based on matrix pencil method," *IEEE Antennas Wireless Propag. Lett.*, vol. 21, pp. 1708–1712, 2022.

[26] R. Moretta, G. Leone, M. A. Maisto, R. Pierri, and R. Solimene, "Array faulty element diagnostics by few phaseless data and convex optimization," in *Proc. 17th Eur. Conf. Antennas Propag. (EuCAP)*, 2023, pp. 1–4.

[27] S. K. Goudos, C. Kalialakis, and R. Mittra, "Evolutionary algorithms applied to antennas and propagation: A review of state of the art," *Int. J. Antennas Propag.*, vol. 2016, no. 1, 2016, Art. no. 1010459.

[28] A. M. Kulkarni, S. S. Pattnaik, and G. Saini, "Genetic-CNN based fault diagnosis in antenna array," in *Proc. IEEE Int. Symp. Antennas Propag. (ISAP)*, 2023, pp. 1–2.

[29] H. M. Yao, M. Li, L. Jiang, K. L. Yeung, and M. Ng, "Antenna array diagnosis using a deep learning approach," *IEEE Trans. Antennas Propag.*, vol. 72, no. 6, pp. 5396–5401, Jun. 2024.

[30] A. J. Van Den Biggelaar, C. J. C. Vertegaal, U. Johannsen, M. Geurts, and A. B. Smolders, "Post-manufacturing calibration procedure for medium-sized silicon-based active phased arrays for mm-wave wireless communications," in *Proc. 14th Eur. Conf. Antennas Propag. (EuCAP)*, 2020, pp. 1–5.

[31] Y. Aslan, P. Aubry, N. B. Onat, J. Janssen, M. Geurts, and A. Yarovoy, "Heuristic over-the-air calibration of beamformer ICs in active mm-wave phased arrays," in *Proc. IEEE Conf. Antenna Meas. Appl. (CAMA)*, 2023, pp. 840–845.

[32] M. Geurts and J. Janssen. "Designing a 5G mmWave antenna means balancing tradeoffs: NXP smarter world blog." 2023. [Online]. Available: https://www.nxp.com/company/about-nxp/smarter-world-blog/BL-DESIGNING-A-5G-MMWAVE

[33] A. Garufo et al., "Mm-wave antennas in package for 5G applications," in *Proc. IEEE ISAP*, 2021, pp. 1–2.

[34] F. A. Musters, R. A. Coesoij, M. D. Migliore, F. Schettino, and M. Spirito, "The antenna dome real-time distributed antenna pattern characterization system," in *Proc. 97th ARFTG Microw. Meas. Conf. (ARFTG)*, 2021, pp. 1–5.

[35] R. A. Coesoij, F. A. Musters, D. Roos, T. van Velden, and M. Spirito, "Calibration approaches in multi-node antenna characterization setups," in *Proc. 100th ARFTG Microw. Meas. Conf. (ARFTG)*, 2023, pp. 1–4.

[36] A. Kannan, "Detection of faulty elements in ic-controlled phased arrays using sparse far-field data," M.S. thesis, Math. Comput. Sci., Delft Univ. Technol., Delft, The Netherlands, 2024.

[37] M. Lange, "Impact of statistical errors on active phased-array antenna performance," in *Proc. IEEE Mil. Commun. Conf. (MILCOM)*, 2007, pp. 1–5.

[38] M. H. Moghaddam, S. R. Aghdam, and T. Eriksson, "Statistical analysis of antenna array systems with perturbations in phase, gain and element positions," in *Proc. IEEE Glob. Conf. Signal Inf. Process. (GlobalSIP)*, 2019, pp. 1–5.

[39] S. Kirkpatrick, C. D. Gelatt, and M. P. Vecchi, "Optimization by simulated annealing," *Science*, vol. 220, no. 4598, pp. 671–680, 1983. [Online]. Available: https://www.science.org/doi/abs/10.1126/science.220.4598.671

[40] C. Guo, W. Hong, H. Lin, and B. Wu, "Planar near-field diagnosis of the large-scale antenna arrays using particle swarm optimization," in *Proc. Asia Conf. Comput. Commun. (ACCC)*, 2020, pp. 20–24.

[41] S. Chatterjee, S. Chatterjee, B. Bandyopadhyay, and A. Majumder, "Simultaneous control of side lobe level and beamwidth in planar array antenna using restricted search evolutionary algorithms," in *Proc. IEEE Asia-Pac. Microw. Conf. (APMC)*, 2019, pp. 673–675.

[42] P. Swain, S. K. Mohanty, and B. B. Mangaraj, "Linear dipole antenna array design and optimization using gravitational search algorithm," in *Proc. 2nd Int. Conf. Adv. Electr., Electron., Inf., Commun. Bio-Informat. (AEEICB)*, 2016, pp. 514–518.

[43] D. E. Goldberg and J. H. Holland, "Genetic algorithms and machine learning," *Mach. Learn.*, vol. 3, pp. 95–99, Oct. 1988.

[44] B.-K. Yeo and Y. Lu, "Fast detection and location of failed array elements using the fast SVM algorithm," in *Proc. 14th Int. Symp. Antenna Technol. Appl. Electromagn. Amer. Electromagn. Conf.*, 2010, pp. 1–4.

[45] M. S. R. A. Coesoij and F. A. Musters, "The antenna dome high-speed characterization system for OTA characterization of FR2 5G active antenna panels," in *Proc. 18th Eur. Conf. Antennas Propag. (EuCAP)*, 2024, pp. 1–5.

[46] M. Raissi, P. Perdikaris, and G. E. Karniadakis, "Physics-informed neural networks: A deep learning framework for solving forward and inverse problems involving nonlinear partial differential equations," *J. Comput. Phys.*, vol. 378, pp. 686–707, Feb. 2019.

[47] R. Palmeri, G. M. Battaglia, A. F. Morabito, S. Costanzo, F. Venneri, and T. Isernia, "Fault diagnosis of realistic arrays from a reduced number of phaseless near-field measurements," *IEEE Trans. Antennas Propag.*, vol. 71, no. 9, pp. 7206–7219, Sep. 2023.

[48] R. Palmeri, T. Isernia, and A. F. Morabito, "Diagnosis of planar arrays through phaseless measurements and sparsity promotion," *IEEE Antennas Wireless Propag. Lett.*, vol. 18, pp. 1273–1277, 2019.

APARNA KANNAN received the Bachelor of Engineering degree in electronics and communications from the College of Engineering, Guindy (part of Anna University) in 2021, and the master's degree in electrical engineering from the Delft University of Technology. She specialized in wireless communication and sensing and was part of the microwave sensing, signals, and systems group during her master's thesis.

NEHIR BERK ONAT received the B.Sc. degree in electrical engineering from the Eindhoven University of Technology in 2019, and the M.Sc. degree (cum laude) from the Signal Processing Systems and Electromagnetics Groups in 2021. He is currently pursuing the Ph.D. degree with the Microwave Sensing, Signals and Systems Group, Delft University of Technology. Afterward, he continued his master's study with the Eindhoven University of Technology as a full-time student, and with the Delft University of Technology as a minor student. He completed his master thesis on performance analysis and array pattern optimization techniques for monostatic and bistatic spaceborne synthetic aperture radar systems.

MARCO SPIRITO (Member, IEEE) received the M.Sc. degree (cum laude) in electrical engineering from the University of Naples Federico II, Naples, Italy, in 2000, and the Ph.D. degree in microelectronics from Delft University of Technology, Delft, The Netherlands, in 2006. From 2000 to 2001, he was a Guest Researcher with Infineon Technologies, Munich, Germany. In 2006, he joined the Department of Electronics and Telecommunications Engineering, University of Naples Federico II. In April 2008, he was an Assistant Professor with the Electronics Research Laboratory, Delft University of Technology, where he has been an Associate Professor since April 2013. In 2010 and 2017, he was one of the co-founder of the Anteverta-MW, Eindhoven, The Netherlands, and Vertigo Technologies, Delft, respectively, two companies pioneering innovative measurement techniques and instruments. His research interests include the development of advanced passive components and building blocks operating in the millimeter and submillimeter frequency ranges, the development of characterization setups and calibration techniques for millimeter and submillimeter waves, and the design and integration of millimeter-wave sensing systems. He was a recipient of the Best Student Paper Award for his contribution to the 2002 IEEE Bipolar/BiCMOS Circuits and Technology Meeting. He was also a recipient of the IEEE Microwave Theory and Techniques Society Microwave Prize in 2008. He was a co-recipient of the Best Student Paper Award at the 2011 IEEE Radio Frequency Integrated Circuits Symposium, the GAAS Association Student Fellowship in 2012, the Best Student Paper Award in second place at the 2018 International Microwave Biomedical Conference, the Best Paper Award at the 2019 Winter ARFTG Conference, and the Best Student Paper Award at the 2019 Summer ARFTG Conference.

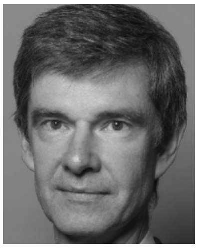

ALEXANDER YAROVOY (Fellow, IEEE) received the Diploma degree (Hons.) in radiophysics and electronics from Kharkov State University, Ukraine, in 1984, and the Candidate Physics and Mathematical Sciences and the Doctor Physics and Mathematical Sciences degrees in radiophysics in 1987 and 1994, respectively. In 1987, he joined the Department of Radiophysics, Kharkov State University as a Researcher, where he became a Full Professor in 1997. From September 1994 to September 1996, he was with the Technidcal University of Ilmenau, Germany, as a Visiting Researcher. Since 1999, he has been with the Delft University of Technology, The Netherlands, where he has been the Chair of the Microwave Sensing, Systems and Signals Group since 2009. He has authored and coauthored more than 500 scientific or technical papers, seven patents, and 15 book chapters. His current research interests include high-resolution radar, microwave imaging, and applied electromagnetics (in particular, UWB antennas). He was a recipient of the European Microwave Week Radar Award for the paper that best advances the state-of-the-art in radar technology in 2001 (together with L. P. Ligthart and P. van Genderen) and in 2012 (together with T. Savelyev). In 2010 together with D. Caratelli and Prof. Yarovoy got the Best Paper Award of the Applied Computational Electromagnetic Society. He served as the General TPC Chair for the 2020 European Microwave Week, the Chair and the TPC Chair for the Fifth European Radar Conference in 2008, and the Secretary for the First European Radar Conference in 2004. He also served as the Co-Chair and the TPC Chair for the Tenth International Conference on GPR 2004. He served as an Associate Editor for IEEE TRANSACTION ON RADAR SYSTEMS and the *International Journal of Microwave and Wireless Technologies* from 2011 to 2018. From 2008 to 2017, he was the Director of the European Microwave Association.

YANKI ASLAN received the B.Sc. degree with double specialization in communications and microwaves/antennas from the Department of Electrical and Electronic Engineering, Middle East Technical University, Ankara, Turkey, in 2014, and the M.Sc. and Ph.D. degrees (cum laude) in electrical engineering from the Delft University of Technology, Delft, The Netherlands, in 2016 and 2020, respectively. Following his Postdoctoral Research with the Microwave Sensing, Signals and Systems Group, Delft University of Technology, he started as an Assistant Professor with TU Delft in April 2021. His current research interests include phased arrays for next-generation communication and sensing systems, array optimization, multibeam antennas, front-end architectures, and beamforming algorithms. He was one of the recipients of the IEEE AP-S Doctoral Research Grant in 2018 and the EuMA Internship Award in 2019.